

Collisionless Accretion of Finite-Angular-Momentum Plasma onto a Spinning Black Hole

John M. Mehlhaff,^{*} Alexander Y. Chen,[†] Martin Luepker,[‡] and Yajie Yuan[§]

Physics Department and McDonnell Center for the Space Sciences,

Washington University in St. Louis; MO, 63130, USA

(Dated: February 26, 2026)

In low-luminosity active galactic nuclei like M87* and Sgr A*, the accretion disk around the central supermassive black hole is tenuous and collisionless. As a result, the usual ideal magnetohydrodynamics (MHD) approximation may not be applicable. In this Letter, we report on the first fully kinetic simulations of the accretion process where the plasma initially has finite angular momentum. The simulated accretion flow behaves remarkably similarly to the magnetically arrested disk (MAD) regime of ideal MHD, reproducing episodes of magnetic flux saturation and eruption typical of MADs. The resemblance to fluid models owes largely to kinetic instabilities, which regulate pressure anisotropy in the disk, allowing fluid terms to dominate the angular momentum transfer. In addition, by handling vacuum regions effectively, our kinetic approach probes the matter supply to the jet funnel. We observe no efficient penetration of the accreting material into this region, which suggests that a pair discharge may be required to sustain the Blandford-Znajek process.

Introduction.— Black hole (BH) accretion powers some of the most fascinating phenomena in the Universe. Accreting supermassive BHs can form active galactic nuclei (AGN), shining brightly across the electromagnetic spectrum [1]. Some AGN even launch powerful, relativistic jets that extend well beyond their host galaxies [2]. Understanding the mechanisms underlying BH accretion and how they convert gravitational potential energy into radiation is an important open problem in astrophysics.

Recently, the Event Horizon Telescope (EHT) used interferometry to image the vicinity of some nearby supermassive BHs, allowing us to see the central engine in action. In particular, the EHT images of M87* [3] and Sgr A* [4] unambiguously identified the BH shadow, and polarization measurements showed strong evidence of ordered magnetic fields near the horizons of both BHs [5, 6]. A major scientific enterprise is interpreting the images to constrain properties of the inner accretion flow. This task relies largely on comparison with synthetic images generated from general relativistic magnetohydrodynamics (GRMHD) simulations [5–8].

However, for low accretion rate systems such as M87* and Sgr A*, the accreting plasma is collisionless [9]. This allows the development of, e.g., nonthermal particle distributions, kinetic plasma instabilities, and multi-temperature components, none of which are captured by GRMHD. For example, to compute radiation from GRMHD simulations, a prescription for the electron temperature inspired by kinetic theory is needed [10–13]. A fully kinetic model would overcome these issues, predicting the accretion dynamics from first principles.

Recently, significant progress has been made toward developing fully kinetic models of BH accretion [14–16]. However, these works have so far been limited to the case of Bondi accretion, with zero initial plasma angular momentum. This precludes a description of the more generic case, where orbiting material must shed its angular mo-

mentum in order to accrete. In view of these former limitations, the recent identification of a finite-angular-momentum kinetic equilibrium in Kerr spacetime [17] represents a major breakthrough. Such an equilibrium can be used as the starting point for fully kinetic simulations of BH accretion with angular momentum transport. In this Letter, we present the first such simulations.

Methods.— We use our GPU-based general relativistic particle-in-cell (GRPIC) code framework *Aperture* [18] to perform fully kinetic, 2D axisymmetric simulations of finite angular momentum plasma accreting onto a BH. The simulations are conducted in horizon-penetrating spherical Kerr-Schild coordinates, $x^\mu = (t, r, \theta, \varphi) = (x^0, x^1, x^2, x^3)$, and assume a dimensionless BH spin of $a = 0.998$. Particles are evolved via the general relativistic equations of motion [19]. Maxwell’s equations are solved under a 3+1 foliation of spacetime [20] involving: the electric current, J^i , computed from the particles; electric and magnetic fields, D^i and B^i , measured by local fiducial observers (FIDOs); and auxiliary metric-induced electric and magnetic fields, E_i and H_i . Several aspects of the 3+1 formalism are detailed in the End Matter; a more complete description, including algorithmic implementation details, is given by [18]. Throughout this work, Greek indices span values 0-3 and Latin indices values 1-3. Unless otherwise stated, all quantities are reported in Lorentz-Heaviside units.

The simulations start from the Luepker Torus, a stable collisionless plasma torus around a rotating BH [17]. The torus is initialized with inner and outer radii, $r_{\text{in}} = 6.2r_g$ and $r_{\text{out}} \approx 73r_g$, respectively. Its density peaks at around $10r_g$ on the equatorial plane. Here, $r_g = GM/c^2$, where M is the BH mass. Additionally, the initial plasma is threaded by a uniform magnetic field described by the vacuum Wald solution [21], with strength B_0 far from the BH. This magnetic field breaks the torus equilibrium by seeding the magnetorotational instability (MRI) [22, 23]

and thus kickstarts the accretion process. The torus is initialized with a maximum $\beta_{\text{pl}} = 2p/b^2$ value of 100 attained near the point of maximum density. Here, p and b are, respectively the plasma pressure and comoving magnetic field strength. Above and below the equatorial pressure maximum, the vertical extent of the torus spans a few MRI wavelengths, λ_{MRI} . We simulate a pure e^\pm pair plasma since it eliminates the electron-ion scale separation. In a GRPIC code, there is no need to maintain a numerical floor on the plasma density, so we leave the region outside the torus a complete vacuum.

We perform two contrasting simulations: one with e^\pm pair production, and one without. In the former, we adopt a simplified pair production scheme to mimic photon-photon pair production near the BH: whenever the Lorentz factor Γ of an electron or positron in the local FIDO frame reaches the threshold $\Gamma_{\text{thr}} = 10$, it emits a photon of FIDO-measured energy $\epsilon_{\text{ph}} = 4m_e c^2$. This photon propagates along a massless geodesic with a fixed probability per timestep of converting into an e^\pm pair. This scheme is identical to what was adopted by [18]. The mean free path for photons to pair-produce is chosen somewhat arbitrarily to be $\ell_{\text{ph}} \approx 2r_g$. When a photon converts into a pair, its energy is evenly distributed between the two resulting particles. Additional information on our numerical setup is provided in the End Matter.

Results. — In both simulations, we observe the development of the MRI in addition to other kinetic instabilities. The MRI triggers accretion at a given location in the torus once it has had time to grow – after approximately one local Keplerian orbit – thereafter leading to the development of a geometrically thick, magnetized, and turbulent accretion flow.

Although weak, the initial vertical magnetic field provides a deep reservoir of magnetic flux. This flux accumulates onto the BH as the result of accretion and eventually saturates, leading to flux eruptions similar to those typically seen in the magnetically arrested disk (MAD) accretion regime [24–27]. Fig. 1 shows a representative snapshot from each of our simulations, taken at the same time $t = 1476r_g/c$. Both simulations show a funnel region consisting of quasi-parabolic field lines anchored to the BH as well as a disk that is mostly magnetically disconnected from the BH.

The most striking feature of Fig. 1 is perhaps the funnel region. In the run without pair production, BH-threading magnetic field lines become a vacuum, with the particles in the accretion disk inhibited from populating them. Devoid of plasma, these field lines exhibit no azimuthal magnetic field, and, hence, do not transmit any Poynting flux. The Blandford-Znajek (BZ) mechanism fails to operate. This agrees with previous findings by [15] but is here seen for the first time in the presence of an accretion flow with finite angular momentum. In contrast, the run with pair production is able to continuously supply plasma to the funnel zone by producing

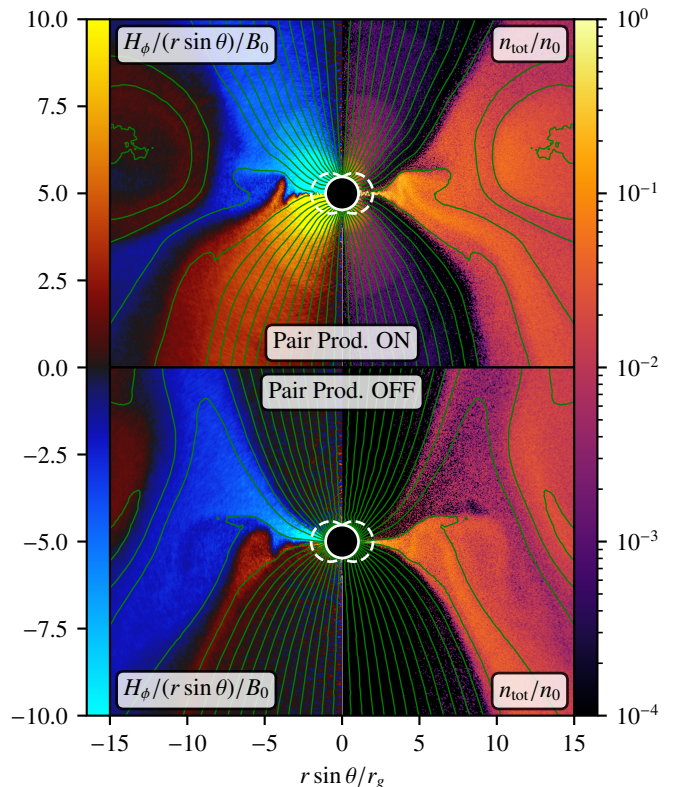


FIG. 1. Snapshots at $t = 1476r_g/c$ of the simulations with and without pair production. Panels display the auxiliary magnetic field component H_φ , and the FIDO-measured total plasma density n_{tot} . As shown in the End Matter, in a steady state, $H_\varphi(r, \theta)$ indicates the electric current through a spherical cap of radius r and half-opening angle θ measured from the $\theta = 0$ axis.

e^\pm pairs via quasi-periodic discharges [28]. Thus, the BZ mechanism operates, extracting energy from the BH as a Poynting-flux-dominated jet.

Fig. 2 shows the magnetic flux, Φ_H , mass accretion rate, \dot{M}_H , and normalized magnetic flux, ϕ , through the event horizon over the duration of the two simulations. In Lorentz-Heaviside units, $\phi = \Phi_H(4\pi/(\dot{M}_H r_g^2 c))^{1/2}$; expressions for Φ_H and \dot{M}_H are given in the End Matter. Both simulations attain a saturation of the normalized flux at around $\phi \sim 50$, after which point a flux eruption is triggered, significantly reducing Φ_H and \dot{M}_H . These eruptions are similar to those seen in GRMHD simulations in the MAD accretion regime. They also resemble eruptions witnessed in kinetic simulations of Bondi accretion [15, 16].

Regardless of whether pair production is active, our simulations show similar saturated ϕ -values and hint at similar eruption recurrence times ($\sim 500r_g/c$). However, the run with pair production takes significantly longer to expel its horizon magnetic flux due to the presence of plasma in the jet funnel. In this run, magnetic balding

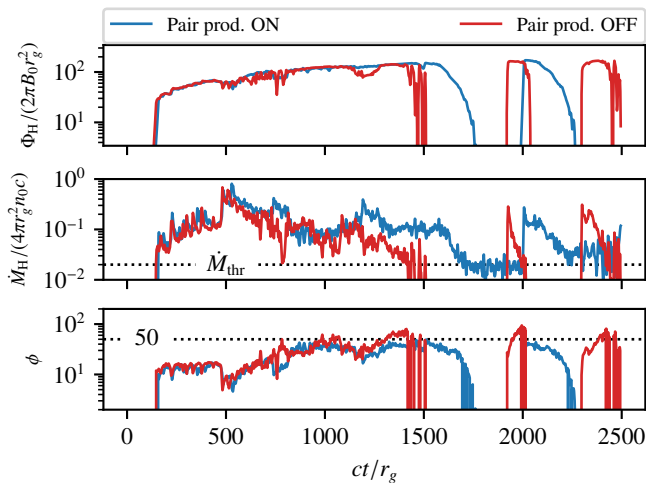


FIG. 2. Horizon-penetrating magnetic flux, Φ_H , mass accretion rate, \dot{M}_H , and normalized flux, $\phi = \Phi_H(4\pi/(\dot{M}_H r_g^2 c))^{1/2}$. To limit noise when calculating ϕ , we exclude times when \dot{M}_H is less than the threshold $\dot{M}_{\text{thr}} = 0.02(4\pi r_g^2 n_0 c)$.

occurs through the reconnection of magnetic field lines across an equatorial current sheet, which tends to yield flux decay timescales $\sim 100 r_g/c$ [16, 29, 30]. In contrast, without pair production, there is no plasma to hold the magnetic field lines in place once the eruption is triggered, and the magnetic flux can escape the BH within a few r_g/c [31].

The most crucial aspect of finite-angular-momentum BH accretion is how the plasma sheds its angular momentum to be able to fall into the BH. We analyze the angular momentum transport in our simulations by isolating contributions from individual stresses following the formalism of [32]. Namely, we split the angular momentum flux term of the stress-energy tensor, T_φ^r , as

$$T_\varphi^r = T_{\text{total}} = T_{\text{plasma}} + T_{\text{Maxwell}} + T_{\text{anisotropy}} + T_{\text{etc}}, \quad (1)$$

where $T_{\text{plasma}} = (\varepsilon + p + b^2)U^r U_\varphi$ is due to the advection of the plasma, $T_{\text{Maxwell}} = -b^r b_\varphi$ is the Maxwell stress, $T_{\text{anisotropy}} = -\Delta p(\hat{b}^r \hat{b}_\varphi - \Delta_\varphi^r/3)$ is the contribution due to pressure anisotropy, and T_{etc} accounts for any additional effects. Here, $\Delta p = p_\perp - p_\parallel$ is the difference between the pressure perpendicular, p_\perp , and parallel, p_\parallel , to the local comoving magnetic field, b^μ . Full definitions and discussions of these terms are included in the End Matter.

In Fig. 3a, we present spacetime diagrams of the angular momentum flux through spherical surfaces, $\dot{L}_s(r, t) = 2\pi \int_0^\pi T_s(r, \theta, t) \sqrt{-g} d\theta$, where s denotes the subscripts in Equation 1. It can be seen that the plasma contribution, \dot{L}_{plasma} , is typically negative, which results from material infall, $U^r < 0$. Negative \dot{L}_{plasma} first appears at a given radius after roughly one local Keplerian period, $2\pi/\Omega_K(r) = 2\pi(r^3/GM)^{1/2}$. This is very close to the local MRI growth rate, demonstrating the role of the MRI in initiating accretion.

Removing the plasma advection term, the rest of the angular momentum transport, $\dot{L}_{\text{total}} - \dot{L}_{\text{plasma}}$, is almost exclusively positive, indicating efficient removal of angular momentum. In particular, the Maxwell stress dominates the outward angular momentum transport in both simulations. Its magnitude is much higher than the contribution from pressure anisotropy when $t > 2\pi/\Omega_K(r)$.

The left panel of Fig. 3b shows a spatial map of β_{pl} for the pair production run. In the jet funnel, β_{pl} is close to 10^{-2} , but it reaches up to 10^2 in the accretion flow. Since $|T_{\text{anisotropy}}/T_{\text{Maxwell}}|$ scales as $|\Delta p|/b^2$ and $|\Delta p|$ is at most $\sim p$, the ratio $|T_{\text{anisotropy}}/T_{\text{Maxwell}}|$ can in principle grow to rival $p/b^2 \sim \beta_{\text{pl}}$. Thus, for the Maxwell stress to dominate the angular momentum transfer even in high- β_{pl} regions indicates that $|\Delta p|$ is regulated to $\ll p$. This can be seen on the right-hand panel of Fig. 3b, where $T_\perp/T_\parallel = p_\perp/p_\parallel$ approaches unity in high- β_{pl} zones.

The regulation of pressure anisotropy in our simulations is imposed by kinetic mirror and firehose instabilities [33]. These are triggered through the global fluid-level dynamics. For example, differential rotation in the disk amplifies the magnetic field, causing T_\perp/T_\parallel to grow due to the conservation of particles' magnetic moments, which leads to mirror threshold violations. Once triggered, mirror and firehose modes scatter particle pitch angles, tending to isotropize the distribution function. As a result, the pressure anisotropy remains largely within the thresholds for these instabilities, as shown in Fig. 3c.

Although Figs. 3b and 3c show the simulation with pair production, we have checked that the run without pair production exhibits similar Δp -regulation. Thus, independently of whether a jet forms, in the accretion disk, kinetic micro-instabilities limit $T_{\text{anisotropy}}$. Additionally, computational resources restrict the separation between long MHD timescales and short micro-instability timescales in our simulations. Kinetic instabilities would operate even faster with respect to global timescales in a real system, all the more firmly enforcing the limits on Δp observed here.

Past 3D works, either involving kinetic shearing-box MRI simulations [34] or global GRMHD simulations with kinetic closures for the pressure anisotropy [35, 36], have typically found $T_{\text{anisotropy}} \lesssim T_{\text{Maxwell}}$. Our result is largely consistent with this. Nevertheless, it is important to extend our work to 3D in order to fully diagnose the dominant angular momentum transport channel.

Finally, we overview the nonthermal particle acceleration in our simulations. We are interested in the particle distribution in several spatial regions: the jet, the equatorial current sheet, and the disk. Similar to GRMHD [12], we define the jet using a magnetization threshold, $\sigma = b^2/2\rho > 0.3$, though we checked that the specific threshold value can be increased or decreased by a factor of ten without modifying our results. Of the zones where $\sigma < 0.3$, we define those lying in the

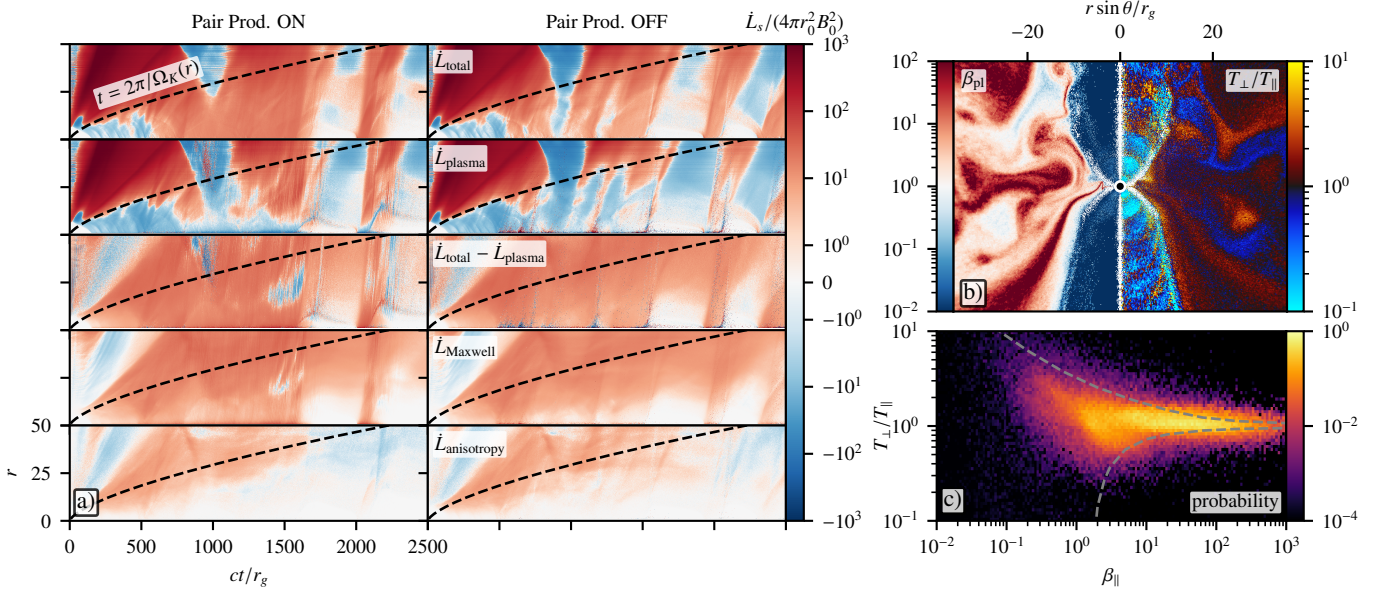


FIG. 3. Panel a): Spacetime diagrams from both simulations (with and without pair production) of the decomposed angular momentum fluxes, \dot{L}_s . Panel b): Spatial maps of β_{pl} and the perpendicular-to-parallel temperature ratio, $T_{\perp}/T_{\parallel} = p_{\perp}/p_{\parallel}$, both pictured at $t = 1476 r_g/c$ in the simulation with pair production. Panel c): Joint probability density of $\beta_{\parallel} = 2p_{\parallel}/b^2$ and T_{\perp}/T_{\parallel} generated from the same simulation snapshot as panel b). Dashed lines indicate where the mirror (top) and firehose (bottom) instability growth rates exceed 10 per cent of the ion cyclotron frequency. Growth rates are calculated semi-analytically via a method detailed in the supplemental material.

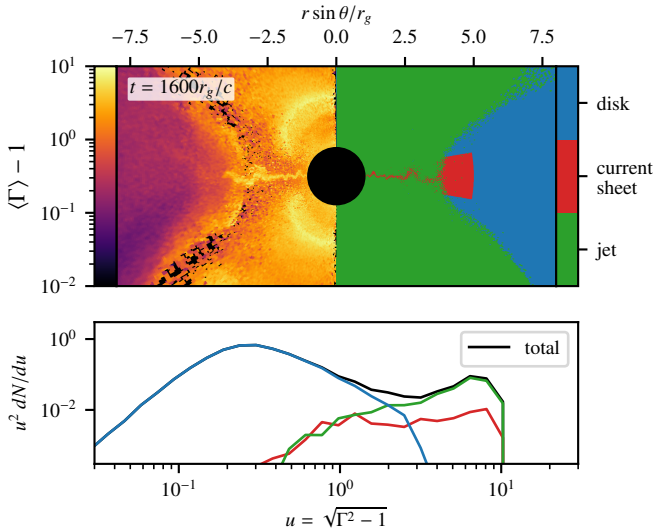


FIG. 4. Top: Maps of the local FIDO-measured average Lorentz factor, $\langle \Gamma \rangle$, and spatial decomposition of the domain into disk, current sheet, and jet regions. Bottom: Contributions to the total particle energy distribution from the different spatial regions. FIDO-measured Lorentz factors Γ and four-velocities u are related through $u = \sqrt{\Gamma^2 - 1}$.

wedge $r_H < r < 5r_g$ and $|\theta - \pi/2| < \pi/18$ as the current sheet; the disk is everywhere else. Fig. 4 shows the total particle distribution decomposed into these spatial regions during a flux eruption. Though the current sheet

is most vigorously accelerating particles at this stage, its contribution to the total spectrum is subdominant to that of the jet funnel (where the pair discharge occurs). The cutoff at $\Gamma = 10$ is due to the pair production threshold. The dominance of the polar region in accelerating pairs has also been found by [15]. However, due to the parallel acceleration in the jet funnel, the particles there have small magnetic pitch angles, so the synchrotron radiation could still be dominated by the current sheet.

Compared to the jet and current sheet, we observe a relative dearth of nonthermal particles in the disk zone of our simulations. The distribution remains mostly thermal in the majority of the accretion flow. In contrast, local box simulations of the MRI turbulence have shown that particles can be accelerated to a nonthermal power law [34, 37]. We believe that this is due in part to our limited scale separation in these global simulations, as well as to their axisymmetric nature, which prevents the MRI turbulence from fully developing. Nevertheless, our results highlight the magnetospheric region as the dominant source of the highest-energy particles.

Particle acceleration operates somewhat differently in the absence of pair production. In this case, no jet develops, and the reconnection current sheet becomes charge starved. While this results in a long nonthermal tail in the distribution extending to $\Gamma \gtrsim 500$, the total plasma energization is smaller. This is likely due to a lower level of magnetic free energy liberated during the flux eruption event when the polar funnel is vacuum-like.

Conclusion.— We have carried out the first global GRPIC simulations of collisionless BH accretion starting from a finite-angular-momentum plasma. In our simulations, the MRI triggers accretion-mediating angular momentum transport – just like in GRMHD. As the plasma evolves, firehose and mirror instabilities limit its pressure anisotropy, providing an effective collisionality that causes the flow to behave like a magnetized fluid. As a result, fluid stresses, specifically magnetic torque, dominate the angular momentum transport. Our simulations also exhibit magnetic flux saturation and eruption phases typical of the MAD accretion state in GRMHD models.

Besides affirming a GRMHD description of angular momentum transport, our kinetic treatment makes several key advancements beyond fluid frameworks. Our code correctly handles vacuum regions and thus probes the role of pair production in enabling a BZ jet. Without pair production, our simulations do not exhibit a mechanism for efficiently mixing plasma from the accretion flow into the near-horizon polar regions. Without a plasma to support the necessary current, no BZ jet is launched.

A kinetic approach also allows us to model and localize nonthermal particle acceleration. We find that the strongest nonthermal particle acceleration occurs in the jet funnel and equatorial current sheet. The accretion flow remains largely thermal in our simulations. Relaxing the assumption of axisymmetry and enhancing the simulations’ dynamic range will enable future work to more thoroughly assess each of the above issues: particle acceleration in the accretion disk, mixing of the accreting plasma into the funnel region, and the dominant angular momentum transport mechanism.

ACKNOWLEDGMENT

We thank Fabio Bacchini, Benoît Cerutti, Luca Comisso, Jason Dexter, Vedant Dhruv, Sasha Philippov, Chris Reynolds, Bart Ripperda, Navin Sridhar, and Dimitri Uzdensky for helpful discussions. JM, ML and YY are supported by a grant from the Simons Foundation (MP-SCMPS-00001470). AC and YY acknowledge support from NSF grants DMS-2235457 and AST-2308111, as well as NASA grant 80NSSC25K0080. AC also acknowledges support from NASA grant 80NSSC24K1095. This work was also facilitated by the Multimessenger Plasma Physics Center (MPPC), NSF grant PHY-2206608 to YY. This research was supported in part by grant NSF PHY-2309135 to the Kavli Institute for Theoretical Physics (KITP). This research used resources of the Oak Ridge Leadership Computing Facility at the Oak Ridge National Laboratory, which is supported by the Office of Science of the U.S. Department of Energy under Contract No. DE-AC05-00OR22725. The authors also acknowledge the Research Infrastructure Services (RIS) group at Washington University in St. Louis for provid-

ing computational resources and services that were used to generate parts of the research results delivered within this paper.

* mehlhaff@wustl.edu

† cyuran@wustl.edu

‡ luepker.m@wustl.edu

§ yaajey@wustl.edu

- [1] D. Lynden-Bell, Galactic Nuclei as Collapsed Old Quasars, *Nature* (London) **223**, 690 (1969).
- [2] R. Blandford, D. Meier, and A. Readhead, Relativistic Jets from Active Galactic Nuclei, *Annu. Rev. Astron.* **57**, 467 (2019), arXiv:1812.06025 [astro-ph.HE].
- [3] Event Horizon Telescope Collaboration, First M87 Event Horizon Telescope Results. I. The Shadow of the Supermassive Black Hole, *Astrophys. J. Lett.* **875**, L1 (2019), arXiv:1906.11238 [astro-ph.GA].
- [4] Event Horizon Telescope Collaboration, First Sagittarius A* Event Horizon Telescope Results. I. The Shadow of the Supermassive Black Hole in the Center of the Milky Way, *Astrophys. J. Lett.* **930**, L12 (2022).
- [5] Event Horizon Telescope Collaboration, First M87 Event Horizon Telescope Results. VIII. Magnetic Field Structure near The Event Horizon, *Astrophys. J. Lett.* **910**, L13 (2021), arXiv:2105.01173 [astro-ph.HE].
- [6] Event Horizon Telescope Collaboration, First Sagittarius A* Event Horizon Telescope Results. VIII. Physical Interpretation of the Polarized Ring, *Astrophys. J. Lett.* **964**, L26 (2024).
- [7] Event Horizon Telescope Collaboration, First M87 Event Horizon Telescope Results. V. Physical Origin of the Asymmetric Ring, *Astrophys. J. Lett.* **875**, L5 (2019), arXiv:1906.11242 [astro-ph.GA].
- [8] Event Horizon Telescope Collaboration, First Sagittarius A* Event Horizon Telescope Results. V. Testing Astrophysical Models of the Galactic Center Black Hole, *Astrophys. J. Lett.* **930**, L16 (2022), arXiv:2311.09478 [astro-ph.HE].
- [9] E. Quataert, W. Dorland, and G. W. Hammett, The Magnetorotational Instability in a Collisionless Plasma, *Astrophys. J.* **577**, 524 (2002), arXiv:astro-ph/0205492 [astro-ph].
- [10] S. M. Ressler, A. Tchekhovskoy, E. Quataert, and C. F. Gammie, The disc-jet symbiosis emerges: modelling the emission of Sagittarius A* with electron thermodynamics, *Mon. Not. R. Astron. Soc.* **467**, 3604 (2017), arXiv:1611.09365 [astro-ph.HE].
- [11] A. Chael, R. Narayan, and M. D. Johnson, Two-temperature, Magnetically Arrested Disc simulations of the jet from the supermassive black hole in M87, *Mon. Not. R. Astron. Soc.* **486**, 2873 (2019), arXiv:1810.01983 [astro-ph.HE].
- [12] P. Z. Yao, J. Dexter, A. Y. Chen, B. R. Ryan, and G. N. Wong, Radiation GRMHD simulations of M87: funnel properties and prospects for gap acceleration, *Mon. Not. R. Astron. Soc.* **507**, 4864 (2021), arXiv:2108.11893 [astro-ph.HE].
- [13] A. Chael, Survey of radiative, two-temperature magnetically arrested simulations of the black hole M87* I: turbulent electron heating, *Mon. Not. R. Astron. Soc.* **537**,

- 2496 (2025), arXiv:2501.12448 [astro-ph.HE].
- [14] A. Galishnikova, A. Philippov, E. Quataert, F. Bacchini, K. Parfrey, and B. Ripperda, Collisionless Accretion onto Black Holes: Dynamics and Flares, *Phys. Rev. Lett.* **130**, 115201 (2023), arXiv:2212.02583 [astro-ph.HE].
- [15] J. Vos, B. Cerutti, M. Mościbrodzka, and K. Parfrey, Particle Acceleration in Collisionless Magnetically Arrested Disks, *Phys. Rev. Lett.* **135**, 015201 (2025), arXiv:2410.19061 [astro-ph.HE].
- [16] E. Figueiredo, J. Mehlhaff, A. Soudais, and B. Cerutti, Emergence of cyclic flux eruptions in kinetic simulations of magnetized spherical accretion onto a Schwarzschild black hole, arXiv e-prints , arXiv:2602.04519 (2026), arXiv:2602.04519 [astro-ph.HE].
- [17] M. Luepker, Y. Yuan, and A. Y. Chen, Stable Collisionless Tori Around Kerr Black Holes, arXiv e-prints , arXiv:2508.09077 (2025), arXiv:2508.09077 [astro-ph.HE].
- [18] A. Y. Chen, M. Luepker, and Y. Yuan, Introducing APERTURE: A GPU-based General Relativistic Particle-in-Cell Simulation Framework, arXiv e-prints , arXiv:2503.04558 (2025), arXiv:2503.04558 [astro-ph.HE].
- [19] F. Bacchini, B. Ripperda, A. Y. Chen, and L. Sironi, Generalized, Energy-conserving Numerical Simulations of Particles in General Relativity. I. Time-like and Null Geodesics, *Astrophys. J. Suppl. Ser.* **237**, 6 (2018), arXiv:1801.02378 [astro-ph.HE].
- [20] S. S. Komissarov, Electrodynamics of black hole magnetospheres, *Mon. Not. R. Astron. Soc.* **350**, 427 (2004).
- [21] R. M. Wald, Black hole in a uniform magnetic field, *Phys. Rev. D* **10**, 1680 (1974).
- [22] S. A. Balbus and J. F. Hawley, A Powerful Local Shear Instability in Weakly Magnetized Disks. I. Linear Analysis, *Astrophys. J.* **376**, 214 (1991).
- [23] S. A. Balbus and J. F. Hawley, Instability, turbulence, and enhanced transport in accretion disks, *Reviews of Modern Physics* **70**, 1 (1998).
- [24] R. Narayan, I. V. Igumenshchev, and M. A. Abramowicz, Magnetically Arrested Disk: an Energetically Efficient Accretion Flow, *Publ. Astron. Soc. Jpn.* **55**, L69 (2003), arXiv:astro-ph/0305029 [astro-ph].
- [25] I. V. Igumenshchev, R. Narayan, and M. A. Abramowicz, Three-dimensional Magnetohydrodynamic Simulations of Radiatively Inefficient Accretion Flows, *Astrophys. J.* **592**, 1042 (2003), arXiv:astro-ph/0301402 [astro-ph].
- [26] A. Tchekhovskoy, R. Narayan, and J. C. McKinney, Efficient generation of jets from magnetically arrested accretion on a rapidly spinning black hole, *Mon. Not. R. Astron. Soc.* **418**, L79 (2011), arXiv:1108.0412 [astro-ph.HE].
- [27] B. Ripperda, M. Liska, K. Chatterjee, G. Musoke, A. A. Philippov, S. B. Markoff, A. Tchekhovskoy, and Z. Younsi, Black Hole Flares: Ejection of Accreted Magnetic Flux through 3D Plasmoid-mediated Reconnection, *Astrophys. J. Lett.* **924**, L32 (2022), arXiv:2109.15115 [astro-ph.HE].
- [28] Y. Yuan, A. Y. Chen, and M. Luepker, Physics of Pair-producing Gaps in Black Hole Magnetospheres: Two-dimensional General Relativistic Particle-in-cell Simulations, *Astrophys. J.* **985**, 159 (2025), arXiv:2503.08487 [astro-ph.HE].
- [29] B. Crinquand, B. Cerutti, G. Dubus, K. Parfrey, and A. Philippov, Synthetic gamma-ray light curves of Kerr black hole magnetospheric activity from particle-in-cell simulations, *Astron. Astrophys.* **650**, A163 (2021), arXiv:2012.09733 [astro-ph.HE].
- [30] A. Bransgrove, B. Ripperda, and A. Philippov, Magnetic Hair and Reconnection in Black Hole Magnetospheres, *Phys. Rev. Lett.* **127**, 055101 (2021), arXiv:2109.14620 [astro-ph.HE].
- [31] R. H. Price, Nonspherical Perturbations of Relativistic Gravitational Collapse. II. Integer-Spin, Zero-Rest-Mass Fields, *Phys. Rev. D* **5**, 2439 (1972).
- [32] E. R. Most, J. Noronha, and A. A. Philippov, Modelling general-relativistic plasmas with collisionless moments and dissipative two-fluid magnetohydrodynamics, *Mon. Not. R. Astron. Soc.* **514**, 4989 (2022), arXiv:2111.05752 [astro-ph.HE].
- [33] M. W. Kunz, J. M. Stone, and E. Quataert, Magnetorotational Turbulence and Dynamo in a Collisionless Plasma, *Phys. Rev. Lett.* **117**, 235101 (2016), arXiv:1608.07911 [astro-ph.HE].
- [34] F. Bacchini, V. Zhdankin, E. A. Gorbunov, G. R. Werner, L. Arzamasskiy, M. C. Begelman, and D. A. Uzdensky, Collisionless Magnetorotational Turbulence in Pair Plasmas: Steady-State Dynamics, Particle Acceleration, and Radiative Cooling, *Phys. Rev. Lett.* **133**, 045202 (2024), arXiv:2401.01399 [astro-ph.HE].
- [35] F. Foucart, M. Chandra, C. F. Gammie, E. Quataert, and A. Tchekhovskoy, How important is non-ideal physics in simulations of sub-Eddington accretion on to spinning black holes?, *Mon. Not. R. Astron. Soc.* **470**, 2240 (2017), arXiv:1706.01533 [astro-ph.HE].
- [36] V. Dhruv, B. Prather, M. Chandra, A. V. Joshi, and C. F. Gammie, Electromagnetic Observables of Weakly Collisional Black Hole Accretion, *Astrophys. J. Lett.* **993**, L33 (2025), arXiv:2510.11365 [astro-ph.HE].
- [37] F. Bacchini, L. Arzamasskiy, V. Zhdankin, G. R. Werner, M. C. Begelman, and D. A. Uzdensky, Fully Kinetic Shearing-box Simulations of Magnetorotational Turbulence in 2D and 3D. I. Pair Plasmas, *Astrophys. J.* **938**, 86 (2022), arXiv:2206.07061 [astro-ph.HE].
- [38] C. K. Birdsall and A. B. Langdon, *Plasma Physics via Computer Simulation* (1991).
- [39] B. Cerutti, A. Philippov, K. Parfrey, and A. Spitkovsky, Particle acceleration in axisymmetric pulsar current sheets, *Mon. Not. R. Astron. Soc.* **448**, 606 (2015), arXiv:1410.3757 [astro-ph.HE].
- [40] <https://github.com/fizban007/Aperture4>.
- [41] T. Z. Esirkepov, Exact charge conservation scheme for Particle-in-Cell simulation with an arbitrary form-factor, *Computer Physics Communications* **135**, 144 (2001).
- [42] A. Y. Chen and A. M. Beloborodov, Electrodynamics of Axisymmetric Pulsar Magnetosphere with Electron-Positron Discharge: A Numerical Experiment, *Astrophys. J. Lett.* **795**, L22 (2014), arXiv:1406.7834 [astro-ph.HE].
- [43] A. Y. Chen, *Particle-in-Cell Simulations and their Applications to Magnetospheres of Neutron Stars*, Ph.D. thesis, Columbia University (2017).
- [44] A. Y. Chen and A. M. Beloborodov, Particle-in-Cell Simulations of the Twisted Magnetospheres of Magnetars. I., *Astrophys. J.* **844**, 133 (2017), arXiv:1610.10036 [astro-ph.HE].

- [45] A. Y. Chen, F. Cruz, and A. Spitkovsky, Filling the Magnetospheres of Weak Pulsars, *Astrophys. J.* **889**, 69 (2020), arXiv:1911.00059 [astro-ph.HE].
- [46] T. H. Stix, *Waves in plasmas* (1992).
- [47] P. Hellinger, P. Trávníček, J. C. Kasper, and A. J. Lazarus, Solar wind proton temperature anisotropy: Linear theory and WIND/SWE observations, *Geophys. Res. Lett.* **33**, L09101 (2006).
- [48] S. D. Bale, J. C. Kasper, G. G. Howes, E. Quataert, C. Salem, and D. Sundkvist, Magnetic Fluctuation Power Near Proton Temperature Anisotropy Instability Thresholds in the Solar Wind, *Phys. Rev. Lett.* **103**, 211101 (2009), arXiv:0908.1274 [astro-ph.SR].

END MATTER

Definitions and Glossary

This paper follows the notation of Komissarov [20] for the Kerr metric and 3+1 formulation. In this section only, we set $G = M = c = 1$. The Kerr-Schild-coordinate metric is given by:

$$ds^2 = g_{tt} dt^2 + 2g_{t\phi} dt d\phi + 2g_{tr} dt dr + g_{rr} dr^2 + g_{\theta\theta} d\theta^2 + g_{\phi\phi} d\phi^2 + 2g_{r\phi} dr d\phi. \quad (2)$$

Notably, there are cross terms for $t\phi$, tr , and $r\phi$. The metric coefficients are:

$$\begin{aligned} g_{tt} &= z - 1, & g_{t\phi} &= -az \sin^2 \theta, & g_{tr} &= z, \\ g_{rr} &= 1 + z, & g_{\theta\theta} &= \rho^2, & g_{\phi\phi} &= \Sigma \sin^2 \theta / \rho^2, \\ g_{r\phi} &= -a \sin^2 \theta (1 + z), \end{aligned} \quad (3)$$

where:

$$\begin{aligned} \rho^2 &= r^2 + a^2 \cos^2 \theta, & z &= 2r / \rho^2, \\ \Sigma &= (r^2 + a^2)^2 - a^2 \Delta \sin^2 \theta, & \Delta &= r^2 + a^2 - 2r. \end{aligned} \quad (4)$$

The lapse function is $\alpha = 1 / \sqrt{1 + z}$; the components of the shift vector are $\beta^r = z / (1 + z)$ and $\beta^\theta = \beta^\phi = 0$. The spatial metric γ_{ij} describes the geometry of a spatial slice at constant t , and it is simply $\gamma_{ij} = g_{ij}$. However, $\gamma^{ij} \neq g^{ij}$. The determinants of γ_{ij} and $g_{\mu\nu}$ are, respectively, g and γ . They are related through $\sqrt{-g} = \alpha \sqrt{\gamma}$.

The *Aperture* code solves Maxwell's equations in curved spacetime:

$$\begin{aligned} \nabla \cdot \mathbf{D} &= \rho, & \text{or} & \quad \frac{1}{\sqrt{\gamma}} \partial_i (\sqrt{\gamma} D^i) = \rho, \\ \nabla \cdot \mathbf{B} &= 0, & \text{or} & \quad \frac{1}{\sqrt{\gamma}} \partial_i (\sqrt{\gamma} B^i) = 0, \\ \frac{\partial \mathbf{D}}{\partial t} &= \nabla \times \mathbf{H} - \mathbf{J}, & \text{or} & \quad \partial_t D^i = e^{ijk} \partial_j H_k - J^i, \\ \frac{\partial \mathbf{B}}{\partial t} &= -\nabla \times \mathbf{E}, & \text{or} & \quad \partial_t B^i = -e^{ijk} \partial_j E_k. \end{aligned} \quad (5)$$

The auxiliary fields E_i and H_i are defined as:

$$\begin{aligned} \mathbf{E} &= \alpha \mathbf{D} + \boldsymbol{\beta} \times \mathbf{B}, & \text{or} & \quad E_i = \alpha \gamma_{ij} D^j + e_{ijk} \beta^j B^k, \\ \mathbf{H} &= \alpha \mathbf{B} - \boldsymbol{\beta} \times \mathbf{D}, & \text{or} & \quad H_i = \alpha \gamma_{ij} B^j - e_{ijk} \beta^j D^k. \end{aligned} \quad (6)$$

Here, e_{ijk} is the 3-dimensional Levi-Civita pseudo-tensor, $e_{ijk} = \sqrt{\gamma} \epsilon_{ijk}$ and $e^{ijk} = \epsilon_{ijk} / \sqrt{\gamma}$, with ϵ_{ijk} the Levi-Civita symbol (entries 1, 0, and -1). The 3-current J^i is related to the 4-current I^μ by $J^i = \alpha I^i$, and the charge density ρ is $\rho = \alpha I^0$. In the absence of significant displacement current, $\partial_t \mathbf{D} \simeq 0$, the field H_φ indicates the electric current through a spherical cap,

$$\begin{aligned} 2\pi H_\varphi(r, \theta) &= 2\pi \int_0^\theta \partial_{\theta'} H_\varphi(r, \theta') d\theta' \\ &= 2\pi \int_0^\theta J^r(r, \theta') \sqrt{\gamma} d\theta', \end{aligned} \quad (7)$$

as mentioned in the caption of Fig. 1.

The particles obey the equations of motion [19]:

$$\begin{aligned} \frac{dx^i}{dt} &= \gamma^{ij} \frac{u_j}{u^0} - \beta^i, \\ \frac{du_i}{dt} &= -\alpha u^0 \partial_i \alpha + u_k \partial_i \beta^k - \frac{u_j u_k}{2u^0} \partial_i \gamma^{jk} + \frac{F_i}{m}, \end{aligned} \quad (8)$$

where F_i is the covariant vector for the Lorentz force:

$$F_i = q \left(\alpha \gamma_{ij} D^j + e_{ijk} \gamma^{jl} \frac{u_l}{u^0} B^k \right). \quad (9)$$

Photons are treated as massless particles that do not experience the Lorentz force.

Following [17], the distribution function of species s is

$$f_s(x^i, u_j, t) = \frac{dN_s}{dV_x dV_u}, \quad (10)$$

where $dV_x = \sqrt{-g} u^0 dr d\theta d\varphi$, $dV_u = du_r du_\theta du_\varphi / (u^0 \sqrt{-g})$, and g denotes the determinant of the metric tensor, $g_{\mu\nu}$. In our axisymmetric simulations, no quantities depend on φ , and so we write $f(x^i, u_j, t) = f(r, \theta, u_j, t)$.

Given the distribution function, one may define the number-flux four-vector,

$$N^\mu(r, \theta, t) = \sum_s \int u^\mu f_s(r, \theta, u_j, t) dV_u, \quad (11)$$

and stress-energy tensor,

$$T^{\mu\nu}(r, \theta, t) = \sum_s m_s \int u^\mu u^\nu f_s(r, \theta, u_j, t) dV_u, \quad (12)$$

where m_s is the rest-mass of a particle of species s . These are the main objects from which we define below most quantities analyzed in the main text.

The magnetic flux and mass accretion rate through the event horizon are

$$\Phi_H = 2\pi \int_0^{\pi/2} B^r(r_H, \theta) \sqrt{\gamma} d\theta \quad \text{and} \quad (13)$$

$$\dot{M}_H = -2\pi \int_0^\pi N^r(r_H, \theta) \sqrt{-g} d\theta. \quad (14)$$

Next, following [32], we define the fluid four-velocity, energy density, pressure, and comoving magnetic field, respectively, as

$$\begin{aligned} U^\mu &= N^\mu / \sqrt{-N^\nu N_\nu}, \\ \varepsilon &= U_\mu U_\nu T^{\mu\nu}, \\ p &= \frac{1}{3} \Delta_{\mu\nu} T^{\mu\nu}, \quad \text{and} \\ b^\mu &= U_\nu {}^* F^{\mu\nu}, \end{aligned} \quad (15)$$

where ${}^*F^{\mu\nu}$ is the dual of the electromagnetic field tensor and $\Delta^{\mu\nu} = U^\mu U^\nu + g^{\mu\nu}$. In addition, we define parallel and perpendicular pressures,

$$\begin{aligned} p_{\parallel} &= \hat{b}_\mu \hat{b}_\nu T^{\mu\nu} \quad \text{and} \\ p_{\perp} &= \frac{1}{2} \left(\Delta_{\mu\nu} - \hat{b}_\mu \hat{b}_\nu \right) T^{\mu\nu}, \end{aligned} \quad (16)$$

where $\hat{b}^\mu = b^\mu/b = b^\mu/(b_\nu b^\nu)^{1/2}$. The total pressure can be written $p = (2p_{\perp} + p_{\parallel})/3$. The pressure anisotropy is $\Delta p = p_{\perp} - p_{\parallel}$. It is bounded by $-3p \leq \Delta p \leq 3p/2$.

Simulation setup

We initialize the Luepker Torus [17] as follows. The torus solution requires specifying four parameters: a fiducial number density scale, n_0 ; a radial scale, r_0 , that corresponds approximately to the location of the number density maximum along the equator; an inner radius, r_{in} ; and a so-called ‘‘energy temperature’’, T , which dictates how quickly the plasma density decays toward the torus edges. The spatial extent of the torus is determined entirely by r_0 and r_{in} . A broader separation between the two increases the maximum energy of the constituent particles, puffing up the equilibrium vertically and extending it radially. A larger torus stores more plasma fuel for accretion at the cost of increasing the simulation domain size needed to contain it.

We choose $r_0 = 12r_g$ and $r_{\text{in}} = 6.2r_g$, which places the torus outer radius at $r_{\text{out}} \approx 73r_g$ and the density maximum at $r = 9.9r_g \sim r_0$. We also select $T = 0.02m_e c^2$, which roughly matches the difference between the maximum and minimum initial particle energies. Finally, we place the inner and outer simulation boundaries, respectively, at $r_{\text{min}} = r_g$ and $r_{\text{max}} = 85r_g$. Choosing r_{min} below the event horizon at $r_{\text{H}} = 1 + \sqrt{1 - a^2} = 1.06r_g$ causally decouples the interior radial boundary from the domain. Our choice of $r_{\text{max}} \gtrsim 1.1r_{\text{out}}$ leaves enough space beyond the torus to fit a perfectly matched layer [38, 39], which absorbs radially outflowing waves and material.

We then select the remaining parameters – B_0 , n_0 , and our grid size N_r – to satisfy a number of constraints, which we outline below. In what follows, we distinguish the fixed parameters B_0 and n_0 from their spatially dependent counterparts, n and B (measured by local FIDOs), by omitting the 0 subscript for the latter.

The first constraint we need to satisfy is that the scale height of the torus, H , be at least several multiples of the most-unstable MRI wavelength, $\lambda_{\text{MRI}} = 2\pi v_A/\Omega_K$. Here, v_A is the Alfvén speed, which, for a given magnetization, $\sigma = B^2/nm_e c^2$, is just $v_A = \sqrt{\sigma/(1 + \sigma)} \simeq \sqrt{\sigma}$, with the nonrelativistic expression $v_A \simeq \sqrt{\sigma}$ holding for $\sigma \ll 1$. In practice, we find that it suffices to enforce $H \gg \lambda_{\text{MRI}}$ at r_0 ; this still creates several MRI

wavelengths per scale height across a healthy range of radii. Furthermore, since our torus is geometrically thick, with $H \sim r$, we phrase this as a requirement on r_0 , namely, $r_0 \gg \lambda_{\text{MRI},0} \equiv 2\pi\sqrt{\sigma_0}/\Omega_K(r_0)$. Given that we have already chosen $r_0 = 12$, guaranteeing that $r_0 \gg \lambda_{\text{MRI},0}$ amounts to a choice of $\sigma_0 = B_0^2/n_0 m_e c^2$. We select $\sigma_0 = 1.8 \times 10^{-4}$, yielding $r_0/\lambda_{\text{MRI},0} = 2\pi\sqrt{r_0\sigma_0}/r_g = 3.4$.

Next, we must ensure that the MRI operates in a fluid regime, growing on a timescale, $\tau_{\text{MRI}} \simeq 1/\Omega_K(r)$, much slower than the magnetic gyration frequency, $\omega_B = eB/m_e c$, of individual particles. Satisfying this requirement by a large margin is important in order for kinetic micro-instabilities to operate on much shorter timescales than the fluid-level MRI [37]. Since r_0 is quite close to the most rapidly orbiting inner edge of the disk, and the initial magnetic field strength is approximately uniform and equal to B_0 , upholding $\tau_{\text{MRI}} \gg 1/\omega_B$ throughout most of the disk can be achieved by enforcing it only at r_0 . We therefore demand that $\omega_{B,0}\tau_{\text{MRI},0} = eB_0/(m_e c\Omega_K(r_0)) \gg 1$. Introducing the fiducial plasma skin depth, $d_0 = (m_e c^2/(n_0 e^2))^{1/2}$, and using the nonrelativistic approximation, $v_A/c = \sqrt{\sigma_0}$, we can rewrite the condition $\omega_{B,0}\tau_{\text{MRI},0} \gg 1$ as $\lambda_{\text{MRI},0}/(2\pi d_0) \gg 1$.

We note that, because d_0 depends only on physical constants and n_0 , and since $\sigma_0 = B_0^2/n_0 m_e c^2$ has already been selected, the choice of $\lambda_{\text{MRI},0}/d_0$ fully constrains both n_0 and B_0 . Our simulations adopt $\lambda_{\text{MRI},0} = 160d_0 \simeq 25(2\pi d_0)$, corresponding to $n_0 = 2000m_e c^2/(e^2 r_g^2)$ and $B_0 = 0.6m_e c^2/(er_g)$. Since d_0 is itself resolved by our simulation grid (outlined below), this means that we resolve $\lambda_{\text{MRI},0}$ with hundreds of grid cells. For comparison, in GRMHD, where it is not necessary to resolve d_0 , the most-unstable MRI mode is typically only resolved by tens of grid cells.

Our final constraint, alluded to above, is that the radial grid spacing, $\Delta r = r\Delta(\ln r) = (r/N_r)\ln(r_{\text{max}}/r_{\text{min}})$, resolve the plasma skin depth, $d = (m_e c^2/(ne^2))^{1/2}$, everywhere. While both quantities vary spatially within the domain, we find this condition to be most stringent where the density reaches its maximum of about n_0 near r_0 . Thus, we only need to require $\Delta r|_{r_0} = r_0\Delta(\ln r) < d_0 = (m_e c^2/(n_0 e^2))^{1/2}$ in order for the skin depth to be resolved everywhere. This can be translated into the condition

$$\begin{aligned} N_r &> \frac{r_0}{d_0} \ln\left(\frac{r_{\text{max}}}{r_{\text{min}}}\right) = \left(\frac{\lambda_{\text{MRI},0}}{d_0}\right) \left(\frac{r_0}{\lambda_{\text{MRI},0}}\right) \ln\left(\frac{r_{\text{max}}}{r_{\text{min}}}\right) \\ &= 2500 \left(\frac{\lambda_{\text{MRI},0}}{160d_0}\right) \left(\frac{r_0}{3.5\lambda_{\text{MRI},0}}\right) \ln\left(\frac{r_{\text{max}}}{80r_{\text{min}}}\right). \end{aligned} \quad (17)$$

To respect this limit, our simulations use $N_r = N_\theta = 4096$ cells in each dimension.

SUPPLEMENTAL MATERIAL

Simulation software

We use the GPU-accelerated PIC code *Aperture* designed for studying relativistic plasmas around compact objects [40]. The code solves the Maxwell-Vlasov system using the standard Particle-in-Cell algorithm on a spherical grid with logarithmic spacing in the r direction. The electromagnetic field is interpolated to the particle position using a first-order spline, then used to update the particle momenta. Particle trajectories are solved using a “drift-kick” approximation, where they are first evolved by a half step according to the geodesic equation, then we apply an electromagnetic push using a modified Boris pusher, and finally they are evolved according to the geodesic equation by another half step. The motion of the particle is used to deposit a current density onto the grid with a first-order shape function using a modified Esirkepov method that conserves charge [18, 41]. Finally, the current is used to update the electromagnetic fields using a semi-implicit predictor-corrector iteration scheme. The code has been successfully applied to perform global simulations of the neutron star magnetosphere in multiple works in the past decade [42–45]. A full description of the code algorithm is contained in reference [18].

Pressure anisotropy and the resulting kinetic instabilities

To obtain the thresholds for mirror and firehose instabilities, we write down the dispersion relation for a plasma with a nonrelativistic bi-Maxwellian distribution at rest in a uniform background magnetic field \mathbf{B}_0 . We use cgs units in this section. The zeroth order distribu-

tion function for species s is

$$f_s(v_{\parallel}, v_{\perp}) = \left\{ \frac{1}{\sqrt{\pi}w_{\parallel}} \exp\left(-\frac{v_{\parallel}^2}{w_{\parallel}^2}\right) \frac{1}{\pi w_{\perp}^2} \exp\left(-\frac{v_{\perp}^2}{w_{\perp}^2}\right) \right\}_s, \quad (18)$$

where v_{\parallel} and v_{\perp} refer to velocities parallel and perpendicular to the background magnetic field, respectively; $w_{\perp s}^2 = 2k_B T_{\perp s}/m_s$ and $w_{\parallel s}^2 = 2k_B T_{\parallel s}/m_s$, with T_{\parallel} and T_{\perp} representing the temperatures in the direction parallel and perpendicular to the background magnetic field, respectively, and k_B the Boltzmann constant. The linearized equations for the Fourier components of the electric field perturbations are

$$\mathbf{k} \times (\mathbf{k} \times \mathbf{E}) + \frac{\omega^2}{c^2} \boldsymbol{\epsilon} \cdot \mathbf{E} = 0, \quad (19)$$

where the dielectric tensor is

$$\boldsymbol{\epsilon}(\omega, \mathbf{k}) = 1 + \sum_s \boldsymbol{\chi}_s(\omega, \mathbf{k}), \quad (20)$$

and $\boldsymbol{\chi}_s$ is the susceptibility of the s -th plasma component. For the bi-Maxwellian distribution (18), the susceptibility tensor can be calculated from [46]

$$\boldsymbol{\chi}_s = \left(\hat{e}_{\parallel} \hat{e}_{\parallel} \frac{2\omega_p^2}{\omega k_{\parallel} w_{\perp}^2} \langle v_{\parallel} \rangle + \frac{\omega_p^2}{\omega} \sum_{n=-\infty}^{\infty} e^{-\lambda} \mathbf{Y}_n(\lambda) \right)_s, \quad (21)$$

where for each species s , the λ parameter is

$$\lambda_s = \frac{k_{\perp}^2 w_{\perp s}^2}{2\Omega_s^2} = \frac{k_{\perp}^2 k_B T_{\perp s}}{m_s \Omega_s^2}, \quad (22)$$

$\omega_{p,s} = \sqrt{4\pi n_s q_s^2/m_s}$ is the plasma frequency, and $\Omega_s = q_s B_0/(m_s c)$ is the cyclotron frequency. For distribution (18), $\langle v_{\parallel} \rangle = 0$ for both species, and the tensor $\mathbf{Y}_n(\lambda)$ is

$$\mathbf{Y}_n(\lambda) = \begin{pmatrix} \frac{n^2 I_n}{\lambda} A_n & -in(I_n - I'_n) A_n & \frac{k_{\perp}}{\Omega} \frac{n I_n}{\lambda} B_n \\ in(I_n - I'_n) A_n & \left(\frac{n^2 I_n}{\lambda} - 2\lambda I'_n + 2\lambda I_n \right) A_n & \frac{ik_{\perp}}{\Omega} (I_n - I'_n) B_n \\ \frac{k_{\perp}}{\Omega} \frac{n I_n}{\lambda} B_n & -\frac{ik_{\perp}}{\Omega} (I_n - I'_n) B_n & \frac{2(\omega - n\Omega)}{k_{\parallel} w_{\perp}^2} I_n B_n \end{pmatrix}, \quad (23)$$

where $I_n(\lambda)$ is the modified Bessel function of the first kind, and

$$A_n = \frac{T_{\perp} - T_{\parallel}}{\omega T_{\parallel}} + \frac{1}{k_{\parallel} w_{\parallel}} \frac{(\omega - n\Omega) T_{\perp} + n\Omega T_{\parallel}}{\omega T_{\parallel}} Z_0(\zeta_n), \quad (24)$$

$$B_n = \frac{(\omega - n\Omega) T_{\perp} + n\Omega T_{\parallel}}{k_{\parallel} \omega T_{\parallel}} \left[1 + \left(\frac{\omega - n\Omega}{k_{\parallel} w_{\parallel}} \right) Z_0(\zeta_n) \right]. \quad (25)$$

Here $\zeta_n = (\omega - n\Omega)/(k_{\parallel} w_{\parallel})$, and

$$Z_0(\zeta) = i\sqrt{\pi} e^{-\zeta^2} (1 + \operatorname{erf}(i\zeta)) \quad (26)$$

is the plasma dispersion function, where $\operatorname{erf}(z) = (2/\sqrt{\pi}) \int_0^z e^{-t^2} dt$ is the error function. We write $\mathbf{n} = c\mathbf{k}/\omega$ and, without loss of generality, assume that the

background field \mathbf{B}_0 is along z and that \mathbf{k} is in the $x-z$ plane with an angle θ with respect to \mathbf{B}_0 . The wave equation (19) then becomes

$$\begin{pmatrix} \epsilon_{xx} - n_z^2 & \epsilon_{xy} & \epsilon_{xz} + n_x n_z \\ \epsilon_{yx} & \epsilon_{yy} - n_x^2 - n_z^2 & \epsilon_{yz} \\ \epsilon_{zx} + n_x n_z & \epsilon_{zy} & \epsilon_{zz} - n_x^2 \end{pmatrix} \begin{pmatrix} E_x \\ E_y \\ E_z \end{pmatrix} = 0. \quad (27)$$

The dispersion relation is obtained by requiring the determinant of the coefficient matrix in (27) to be zero:

$$\det \begin{pmatrix} \epsilon_{xx} - n_z^2 & \epsilon_{xy} & \epsilon_{xz} + n_x n_z \\ \epsilon_{yx} & \epsilon_{yy} - n_x^2 - n_z^2 & \epsilon_{yz} \\ \epsilon_{zx} + n_x n_z & \epsilon_{zy} & \epsilon_{zz} - n_x^2 \end{pmatrix} = 0. \quad (28)$$

For our applications, we consider a pair plasma, so the ion-to-electron mass ratio is $m_i/m_e = 1$. We also assume that both species have the same density and temperatures, so $\beta_{\parallel i} = \beta_{\parallel e}$ and $T_{\perp i}/T_{\parallel i} = T_{\perp e}/T_{\parallel e}$. The dispersion relation is then fully determined by the following parameters: $\beta_{\parallel i}$, $T_{\perp i}/T_{\parallel i}$ and the ion magnetization $\sigma_i = B_0^2/(4\pi n_i m_i c^2)$. We consider the low- σ_i regime as appropriate for the accretion disk. It turns out that as long as

$\sigma_i \ll 1$, or, more precisely, $k_B T_{\parallel i}/(m_i c^2) = \beta_{\parallel i} \sigma_i/2 \ll 1$, the growth rate of mirror and firehose instabilities does not depend on the exact value of σ_i . In our calculations, we typically fix σ_i at a small value between 10^{-4} and 10^{-2} .

In practice, it appears that the oblique firehose and mirror instabilities constrain the plasma anisotropy (e.g., [47, 48]). These are non-propagating instabilities, meaning that ω is purely imaginary. To find the growth rate of these instabilities at a given $\beta_{\parallel i}$, $T_{\perp i}/T_{\parallel i}$ and \mathbf{k} , we employ the `FindRoot` function in `Mathematica` to solve for ω in the dispersion relation (28). We use Newton's method with a purely imaginary starting trial solution, which usually works well as long as the trial solution is not too far from the true solution. Then, for a given set of $\beta_{\parallel i}$ and $T_{\perp i}/T_{\parallel i}$, we scan \mathbf{k} in both its magnitude k and its angle θ with respect to \mathbf{B}_0 to obtain the maximum growth rate of the instability. Finally, we find the maximum growth rate as a function of $T_{\perp i}/T_{\parallel i}$ for a given $\beta_{\parallel i}$, and locate the $T_{\perp i}/T_{\parallel i}$ value that gives a maximum growth rate of 10% the ion cyclotron frequency, which we illustrate in panel c) of Fig. 3 in the main text.